CFD Study on Taylor Bubble Characteristics in Carreau-Yasuda Shear Thinning Liquids

Somasekhara Goud Sontti and Arnab Atta (iD) *

Multiscale Computational Fluid Dynamics (mCFD) Laboratory, Department of Chemical Engineering, Indian Institute of Technology Kharagpur, West Bengal 721302, India

In the present study, Taylor bubble formation in two-phase gas-non-Newtonian Carreau liquid flowing through a confined co-flow microchannel is investigated. Systematic analyses are carried out to explore the influences of rheological properties, inlet velocities, and surface tension on Taylor bubble length, shape, velocity, and liquid film thickness. Aqueous solutions of carboxymethyl cellulose (CMC) with different mass concentrations are considered as the non-Newtonian liquids to understand the fundamentals of flow behaviour. With increasing solution viscosity and liquid phase inlet velocity, Taylor bubble formation frequency and velocity increased; however, the bubble length was found to decrease. Velocity profiles inside the Taylor bubble and liquid slug were analyzed, and distinct velocity distributions were found for different CMC concentrations. Flow regime maps are developed based on gas and liquid velocities for Carreau liquids in the co-flow microchannel. This study essentially provides useful guidelines in designing a non-Newtonian microfluidic system for precise control and manipulation of Taylor bubbles.

Keywords: microchannel, shear thinning liquid, Taylor bubble, co-flow, CFD

INTRODUCTION

Over the last two decades, studies on segmented flow in microchannels have gained vast interest due to their wide range of applications in microfluidics, lab-on-a-chip devices, and microreactors.[1,2] Two-phase flow patterns are generally classified as bubbly, Taylor, churn, annular, and stratified flow. Taylor bubble flow is one of the important two-phase flow patterns, where elongated bubbles are separated by liquid slug, and is characterized by a length larger than the equivalent diameter of the microchannel. Significant advantages of the Taylor bubble flow are its superior heat and mass transfer performance, which are distinguished by interfacial area and internal circulation.[3–6] These parameters are determined by the bubble length, near-wall liquid film thickness, and velocity field inside the Taylor bubble and liquid. Internal circulatory flow patterns enhance convective mass transport, and reduce axial dispersion.[7] Various microfluidic devices are available to generate bubble/droplets, out of which the co-flow device is one of the simplest microfluidic configurations typically utilized for Taylor bubble formation. In the co-flow device, the dispersed phase gas is introduced through a small micro capillary into the main microchannel, where the continuous phase liquid is flowing in the same direction. To obtain the desired segmented flow, specific ranges of flow rates for both phases are essential. Numerous studies have proposed various flow regimes for different flow conditions in microchannels.[8–10] Salman et al.[11] experimentally and theoretically investigated Taylor bubble formation in a co-flow device for an air-octane system. Three different mechanisms of bubble breakup and coalescence were observed at low liquid flow rates. A theoretical model was developed to predict the Taylor bubble length formed by various breakup mechanisms, and the model predictions were found to conform well with experiential results. To identify the interface between two phases, several numerical models have been developed, such as front-tracking (FT),[12] volume of fluid (VOF),[13,14] level set (LS),[15]

phase field,[16] and the Lattice Boltzmann method (LBM).[17,18] Yu et al.[19] performed experiments and LBM simulations of gas-liquid flow in flow-focusing and converging shaped microchannels. The bubble length, shape, and formation mechanism were studied under different operating conditions and mixer configurations. They identified bubbly and slug flow regimes depending on the capillary number (Ca). Chen et al.[20] numerically investigated Taylor bubble flow in a co-flow device using the LS method. Numerical predictions of liquid film thickness, bubble length, shape, and pressure drop were found to be in good agreement with the experimental results of Bretherton.[21] Goel and Buwa[22] explored the bubble formation in a circular microchannel using the VOF approach. The effect of inlet velocities, channel diameter, and wall adhesion properties on the Taylor bubble formation were analyzed. Gupta et al.[23] critically analyzed Taylor bubble flow in a co-flow device, and provided guidelines to capture thin liquid film around the bubble by imposing refined mesh in the vicinity of wall. Wang[24] also applied the VOF method to understand Taylor bubble flow for an air-water system in a tapered co-flow configuration, where the effects of inlet velocities and capillary injection length on Taylor bubble length and formation frequencies were described.

From the literature, it is apparent that most of the efforts are devoted in understanding and modelling of the Taylor flow hydrodynamics and its characteristics associated with Newtonian liquids at the microscale. However, the fluid behaviour of non-Newtonian shear thinning fluids is known to be different

from that of Newtonian fluid, as the viscosity depends on the shear rate.[25,26] In reality, many commercial chemicals (e.g., colloidal suspensions and polymer solutions) and biological samples (e.g., blood and DNA solutions) exhibit non-Newtonian shear thinning and viscoelastic characteristics.[27] Bubble formation and breakup dynamics in such liquids are complex due to non-Newtonian characteristics of liquid phase.[28] Consequently, the fundamental studies of two-phase flow involving non-Newtonian fluids are of paramount interest. Recently, considerable attention has been devoted to gain insights into the effect of non-Newtonian rheological properties on two-phase flow and characteristics in different microfluidic configurations.[29–32] Fu et al.[30] experimentally investigated Taylor bubble formation in T-junction microchannels using various concentrations of polyacrylamide (PAAm) solutions, and reported different flow regimes by varying gas and liquid operating conditions. It is evident from their results that the Taylor bubble length increases nonlinearly with the gas-liquid flow rate ratios, and decreases with PAAm concentration. Chen et al.[31] numerically studied bubble formation using the VOF method in a T-junction micro-device for non-Newtonian liquids. Initially, their computational model was verified for an air-water system with in-house experimental flow visualization observations. Thereafter, the numerical model was extended for non-Newtonian liquids. Considering liquid phase as a yield stress fluid, Laborie et al.[32] explored bubble formation in T-junction and flow-focusing microchannels and developed phase diagrams for bubble generation. Wang et al.[33] also analyzed two-phase flow regimes in a T-junction microchannel using a gas-carboxymethyl cellulose (CMC) system. Various flow patterns such as slug, slug-annular, and annular flow were observed. We have recently reported Taylor bubble flow behaviour in a co-flow microchannel with Newtonian and power-law liquids using a VOF model.[34] Various mass concentrations of CMC were taken as the non-Newtonian liquid phase, and the results showed that in the presence of CMC, bubble length decreased. We have also delineated flow pattern maps in a co-flow device based on gas and liquid phase inlet velocities for power-law liquids.[35] The present work aims to investigate the characteristics of Taylor bubble flow in high viscous liquids. Taylor bubble formation in non-Newtonian CMC solutions is studied using a CFD model based on finite volume approach. To understand the underlying physics of Taylor bubble formation in shear thinning liquids, a Carreau-Yasuda viscosity model is considered, which has not been addressed earlier in the literature. To realize the non-Newtonian flow characteristics associated with Taylor bubbles, the effects of rheological properties, continuous inlet velocity, and surface tension are analyzed by examining the bubble length, velocity, shape, liquid film thickness, and velocity field distribution inside the Taylor bubble.

NUMERICAL MODEL

The physical process of multiphase flow system is typically described by a set of conservation equations like mass, momentum, and a marker function to distinguish the fluid-fluid interface. As discussed in the previous section, there are various interface capturing methods available with their own benefits and drawbacks. The VOF method is most popular due its simplicity but at the same time it is precise enough that accounts for substantial curvature changes of the interface.[12,36–39] It has also been proven that the VOF method accurately traced the interface with relatively lesser computational effort.[12] In our previous works, we also had implemented the VOF method for Taylor bubble

formation in Newtonian and non-Newtonian systems.[34,40] Accordingly, in this work, the VOF method is further exercised for Carreau liquids, and the following set of governing equations are solved to identify the interface in the computational domain.

Volume of Fluid (VOF) Method

A single set of conservation equations is computed for immiscible fluids in the VOF approach. The set of governing equations and formulation of VOF method for multiphase flow system are as follows:[13]

Equation of continuity:

$$\frac{\partial \rho}{\partial t} + \nabla.(\rho \vec{U}) = 0 \tag{1}$$

Equation of motion:

$$\frac{\partial(\rho \vec{U})}{\partial t} + \nabla.(\rho \vec{U}\vec{U}) = -\nabla P + \nabla.\bar{\bar{\tau}} + \rho \vec{g} + \vec{F}_{SF} \tag{2}$$

$$\bar{\bar{\tau}} = \eta \dot{\gamma} = \eta(\nabla \vec{U} + \nabla \vec{U}^T) \tag{3}$$

where $\vec{U}$ is the velocity vector, ρ is the density, η is the dynamic viscosity, P is the pressure, $\vec{g}$ is the gravitational acceleration, and $\vec{F}_{SF}$ is the volumetric surface tension force.

For a two-phase flow system, if the fluid phases are denoted by the subscripts and the volume fraction (C) of the secondary phase is known, then the fluid properties such as, density and viscosity in the computational domain are calculated by:

$$\rho = C_2\rho_2 + (1 - C_2)\rho_1 \tag{4}$$

$$\eta = C_2\eta_2 + (1 - C_2)\eta_1 \tag{5}$$

Equation of marker function:
In the VOF approach, the interface between gas-liquid phases can be identified by solving the following advection equation:

$$\frac{\partial C_q}{\partial t} + (\vec{U}_q.\nabla C_q) = 0 \tag{6}$$

where q denotes either the gas or liquid phase. $C_q = 0$ denotes an empty cell and $C_q = 1$ designates a computational cell completely filled with q phase. The interface is identified by condition $0 < C_q < 1$. The volume fraction of the primary phase is obtained from the following equation:

$$\sum C_q = 1 \tag{7}$$

Continuum surface tension (CSF) model:
The continuum surface force (CSF) model[41] has been used in this work to incorporate the surface tension force ($\vec{F}_{SF}$), which is added in the momentum equation (Equation (2)) as a source term for two-phase flows, and can be represented as:

$$\vec{F}_{SF} = \sigma \kappa_n \left[\frac{C_1\rho_1 + C_2\rho_2}{\frac{1}{2}(\rho_1 + \rho_2)} \right] \tag{8}$$

where σ denotes the surface tension and κ_n is the radius of curvature. According to the CSF model,[41] κ_n is defined in terms of unit normal $\hat{N}$ as follows:[42]

$$\kappa_N = -\nabla.\hat{N} = \frac{1}{|\vec{N}|} \left[\left(\frac{\vec{N}}{|\vec{N}|}.\nabla \right) |\vec{N}| - \left(\nabla.\vec{N} \right) \right] \tag{9}$$
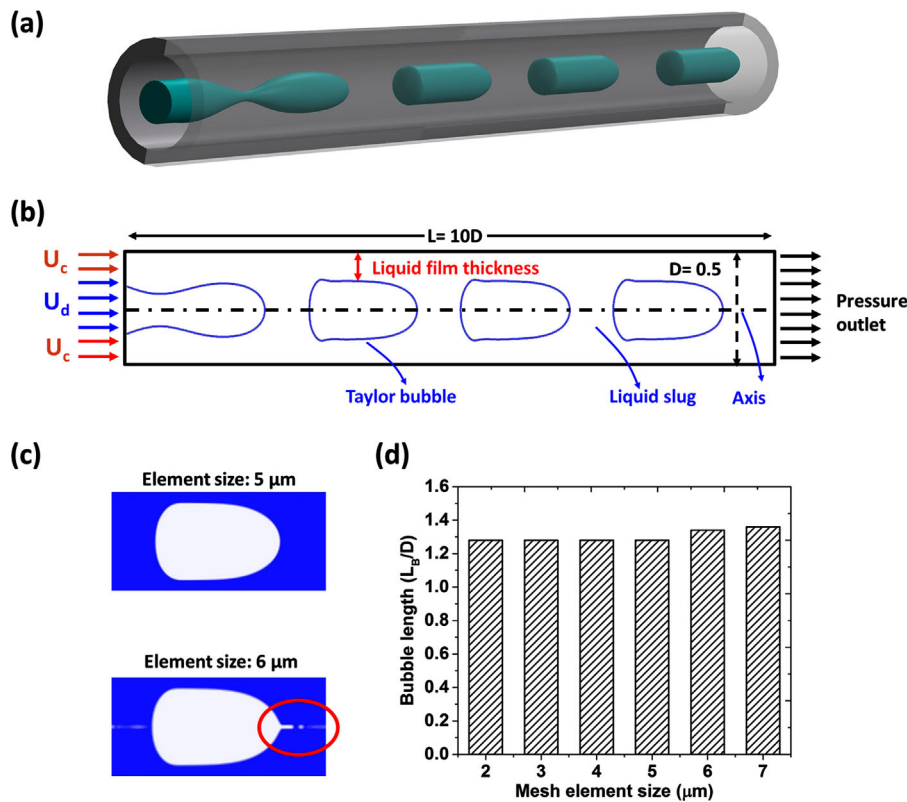
Figure 1. (a) 3D illustration of the Taylor bubble formation in circular co-flow device, (b) 2D representation of the computational model with boundary conditions, (c) interface tracking comparison between two different mesh element sizes (5 versus 6 μm), highlighting elongated thread in coarse mesh (6 μm), and (d) grid independence study of the bubble length for air-CMC-1.0 % system for $U_G = 0.5$ m/s, $U_L = 0.5$ m/s.

where $\hat{N} = \frac{\vec{N}}{|\vec{N}|}$, and $\vec{N} = \nabla C_q$.

Furthermore, the surface normal can be expressed in terms of three phase contact angle (θ_w) at the wall as:

$$\hat{N} = \hat{N}_w cos\theta_w + \hat{M}_w sin\theta_w \tag{10}$$

where $\hat{N}$ and $\hat{M}$ are the unit normal vector and tangential vector to the wall, respectively.[42]

Constitutive equation of continuous phase

To implement shear thinning nature of the liquid phase, the Carreau-Yasuda viscosity model[43] has been adopted, where the effective viscosity (η_{eff}) is expressed as:

$$\eta_{eff} = \eta_\infty + \left(\eta_0 - \eta_\infty\right)\left[1 + \left(\lambda\dot{\gamma}\right)^2\right]^{\frac{n-1}{2}} \tag{11}$$

where $\dot{\gamma}$ is the applied shear rate, η_0 represents the dynamic viscosity corresponding to the zero shear rate ($\dot{\gamma} \mapsto 0$), and η_∞ is the viscosity at infinite shear rate ($\dot{\gamma} \mapsto \infty$), which was assigned as
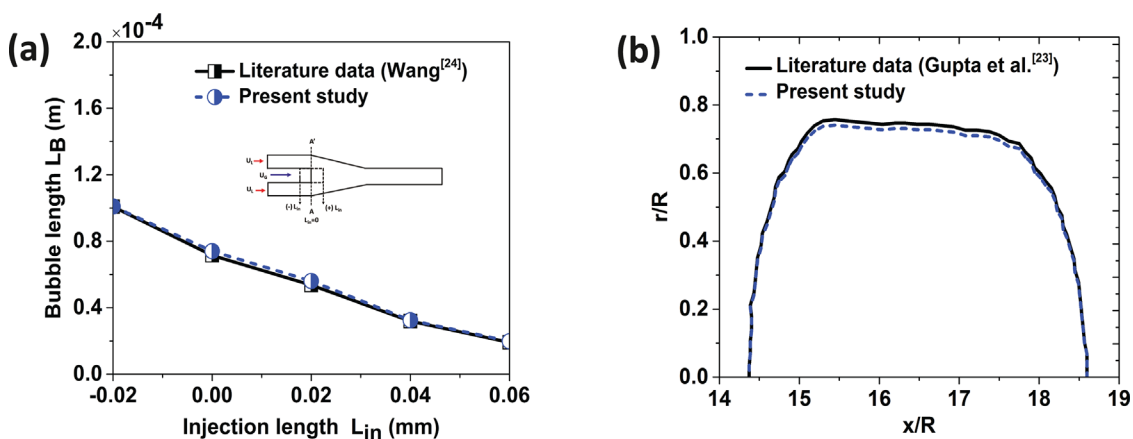

Figure 2. (a) Taylor bubble length comparison for different injection lengths (L_{in}) for $\eta_w = 1.003 \times 10^{-3}$ kg/m.s, $Q_G = 0.47$ μL/s, and $Q_L = 2.01$ μL/s with the results of Wang,[24] and (b) comparison of Taylor bubble shape with Gupta et al.[23] for air-water system with $U_G = 0.5$ m/s, $U_L = 0.5$ m/s.

Table 1. Rheological properties of Carreau-Yasuda viscosity model for different CMC solutions[46]

CMC (wt%)	ρ (kg/m^3)	η_0 (Pa.s)	η_∞ (Pa.s)	λ (s)	n (–)	σ (N/m)
0.1	996.28	0.0091	0.001	0.0214	0.87	0.072
0.4	995.39	0.1102	0.001	0.1099	0.67	0.072
0.6	994.13	0.3602	0.001	0.1828	0.57	0.072
1.0	993.61	2.9899	0.001	0.3653	0.40	0.072

the liquid viscosity. The parameter λ denotes the relaxation time, and n is the flow behaviour index.

Computational Model

A 3D illustration of Taylor bubble formation in a circular co-flow micro-device is shown in Figure 1a, where the Taylor bubbles are separated by a thin liquid film adjacent to the solid wall. In this work, a circular microchannel of diameter (D) 0.5 mm, and a length of 10 D is considered. The selection of $L/D = 10$ is based on the modelling guideline and practice followed by previous researchers.[23,34,44,45] Our preliminary simulations also indicate that a higher ratio than $L/D = 10$ does not induce any significant influence on Taylor bubble length, velocity, and surrounding film thickness for the considered ranges of operating conditions. The computational domain is taken into account as a two-dimensional axisymmetric geometry (Figure 1b). Transient simulations are carried out in a finite volume method based solver. To solve the aforementioned partial differential equations, commercial software ANSYS Fluent 17.0 is used. The pressure-velocity coupling is solved by the fractional step method (FSM) using a first order implicit non-iterative time advancement (NITA) scheme.[42]

The momentum equation is resolved by quadratic upstream interpolation for convective kinetics (QUICK) scheme and volume fraction equation is solved using geo-reconstruct method. In the present study, fixed Courant number (Co = 0.25) and variable time step are utilized. Constant velocity boundary condition is considered at the liquid and gas inlets, and the pressure boundary is set at the outlet. No-slip condition is assumed at the channel wall. Additional details on the model implementation can be found in our earlier work.[34] At first, the grid independence test was conducted with various mesh sizes, ranging from 7–2 μm. Smooth gas-liquid interface was not captured in simulations with coarser grids (6 and 7 μm), and Figure 1c illustrates the appearance of elongated thread at the nose of Taylor bubble in such cases. Figure 1d demonstrates the influence of grid size on the Taylor bubble length, which did not change with mesh sizes below 5 μm under identical operating conditions. Therefore, in the present study, the optimum grid size is considered to be 5 μm. For precise tracking of the gas-liquid interface and to estimate the liquid film thickness around the Taylor bubble, near wall mesh refinement is carried out as per the guidelines of Gupta et al.[23] Subsequently, the predicted liquid film thickness in the near wall region is analyzed.

RESULTS AND DISCUSSION

At first, the CFD model is corroborated with the literature data of Wang[24] and Gupta et al.[23] for air-water two-phase flow systems in co-flow microchannels. For validation with Wang,[24] a tapered co-flow configuration is simulated. The model predictions of bubble length are found to be in excellent agreement with literature data, as shown in Figure 2a. Furthermore, the Taylor bubble shape in a straight circular microchannel is compared with the results of Gupta et al.[23] to reinforce credibility of the developed model. Notably, for Ca = 0.006, the Taylor bubble velocity (0.55 m/s) and shape are in good agreement with literature data, as shown in Figure 2b.
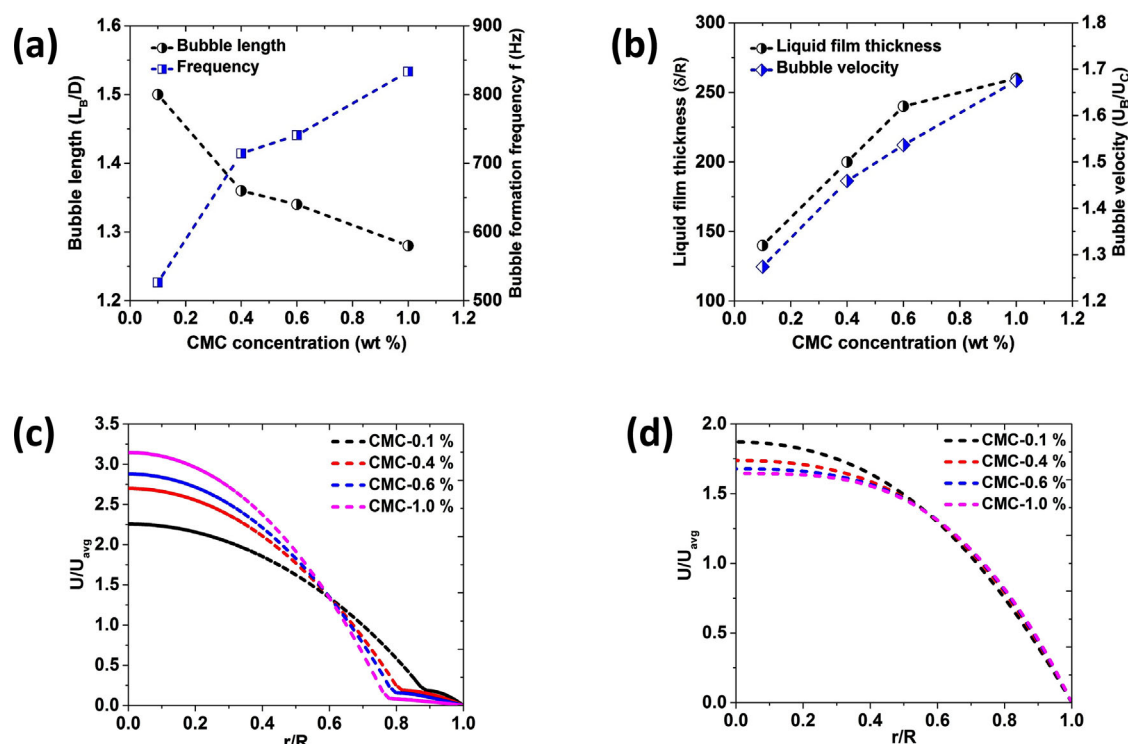

Figure 3. Effect of CMC concentration on: (a) non-dimensional bubble length and formation frequency, (b) surrounding liquid film thickness, (c) velocity profile in the middle of a Taylor bubble, and (d) velocity profile in the middle of a liquid slug at U_L = 0.5 m/s and U_G = 0.5 m/s.
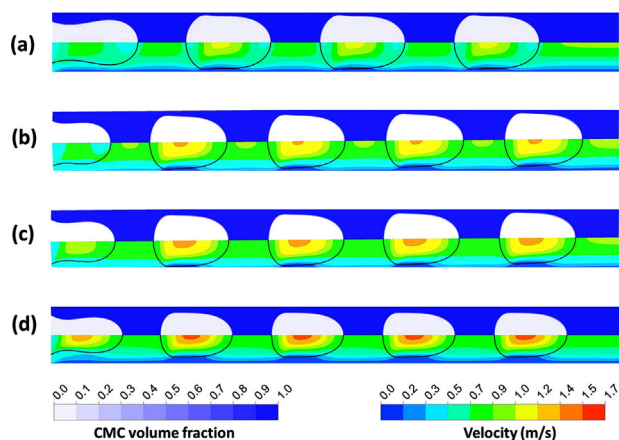
Figure 4. Effect of CMC concentration on velocity distribution (upper halves are volume fraction and lower halves are velocity field) for: (a) CMC-0.1 %, (b) CMC-0.4 %, (c) CMC-0.6 %, and (d) CMC-1.0 % at U_L = 0.5 m/s and U_G = 0.5 m/s.

Figure 6. Non-dimensional bubble length as a function of modified capillary number for different CMC solutions at U_L = 0.5 m/s and U_G = 0.5 m/s.

These two validations with independent sources advocate the efficacy of this model, and are extended for the present study.

Effect of Carboxylmethyl Cellulose (CMC) Concentration

At first, the effect of CMC concentration on Taylor bubble flow has been systematically studied. To understand the rheological properties using the Carreau-Yasuda viscosity model, we have considered four different mass concentrations of CMC in water. Physical properties of different CMC solutions are obtained from the experimental data of Sousa et al.,[46] and are summarized in Table 1.

It can be noted from Table 1 that the surface tension value is identical for all solutions, which is similar to that of water. To understand the viscous effects of non-Newtonian liquids, the effective viscosity (η_{eff}) is calculated based on the rheological properties (Equation (12)[47]), and the influence of CMC concentration on Taylor bubble formation is explained based on η_{eff} of the continuous phase.

$$\eta_{eff} = (\eta_0 - \eta_\infty)\lambda^{n-1}\left(\frac{3n+1}{4n}\right)^n\left(\frac{8U_L}{D}\right)^{n-1} \tag{12}$$

where η_0 is the consistency index, U_L is the liquid velocity, D is capillary diameter, and n is the power-law index, respectively.

Figure 3a shows that on increasing CMC concentration, Taylor bubble length decreases, and the formation frequency increases due to increasing effective viscosity of the liquid phase. A thin liquid film around the Taylor bubble is precisely captured, which is measured from the wall to the middle of the bubble. Surrounding liquid film thickness is observed to increase, as shown in Figure 3b. Consequently, Taylor bubble velocity increases due to increase in liquid film thickness and change in the bubble shape/nose curvature, which decreases with increasing CMC concentration. A detailed insight on velocity fields inside the Taylor bubble and liquid slug are necessary to understand the heat and mass transfer performance. To realize the viscous effects, non-dimensional velocity profiles are analyzed in the middle of the Taylor bubble and liquid slug, and are illustrated in Figure 3c and d, respectively.

The velocity inside a Taylor bubble is found to increase with increasing CMC concentration, as shown in Figure 3c. Liquid film thickness surrounding the bubble is characterized by a discontinuous velocity field at the gas-liquid interface. Figure 3d depicts the effect of CMC concentration on the continuous liquid phase velocity profiles in the liquid slug. In the case of lower concentrations, the nearly parabolic profile is observed in the liquid slug. However, a relatively flatter profile is depicted at the higher concentration, which is the typical characteristic of shear thinning liquids. Figure 4 illustrates that with increasing CMC concentration, the velocity field inside the Taylor bubble significantly increases, which corresponds to the quantitative analyses in Figure 3c. Subsequently, the non-homogeneous viscosity variation in the microchannel is analyzed for considered CMC solutions. From Table 1 and Equation (12), it is apparent that the effective viscosity increases with increasing concentration of CMC. Figure 5 describes viscosity variation along with phase fraction for various CMC solutions, and as expected, this phenomena
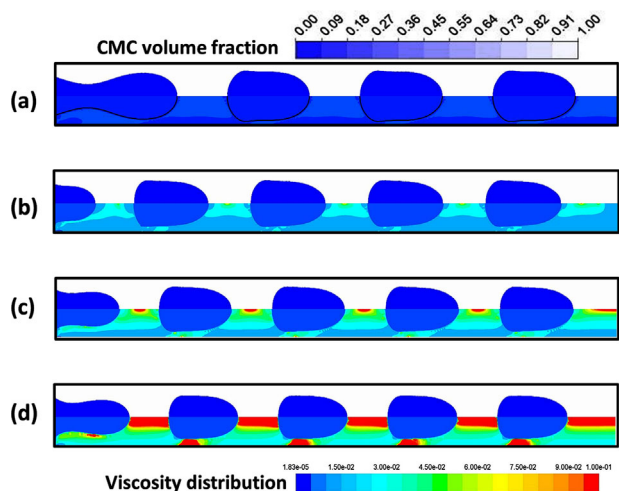

Figure 5. Effect of CMC concentration on non-homogeneous viscosity distribution (upper halves are volume fraction and lower halves are viscosity distribution) for: (a) CMC-0.1 %, (b)CMC-0.4 %, (c) CMC-0.6 %, and (d) CMC-1.0 % at U_L = 0.5 m/s and U_G = 0.5 m/s.
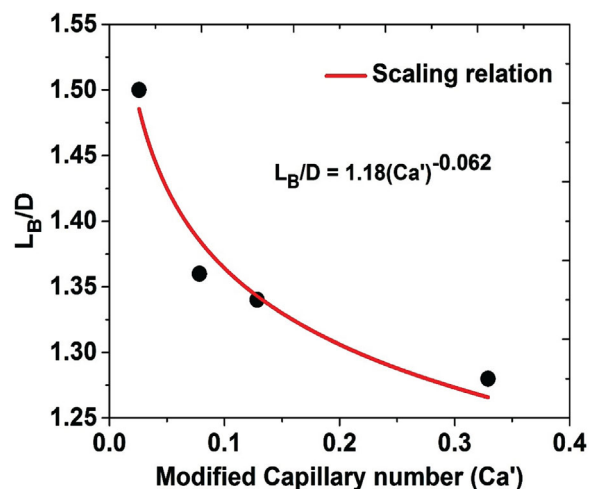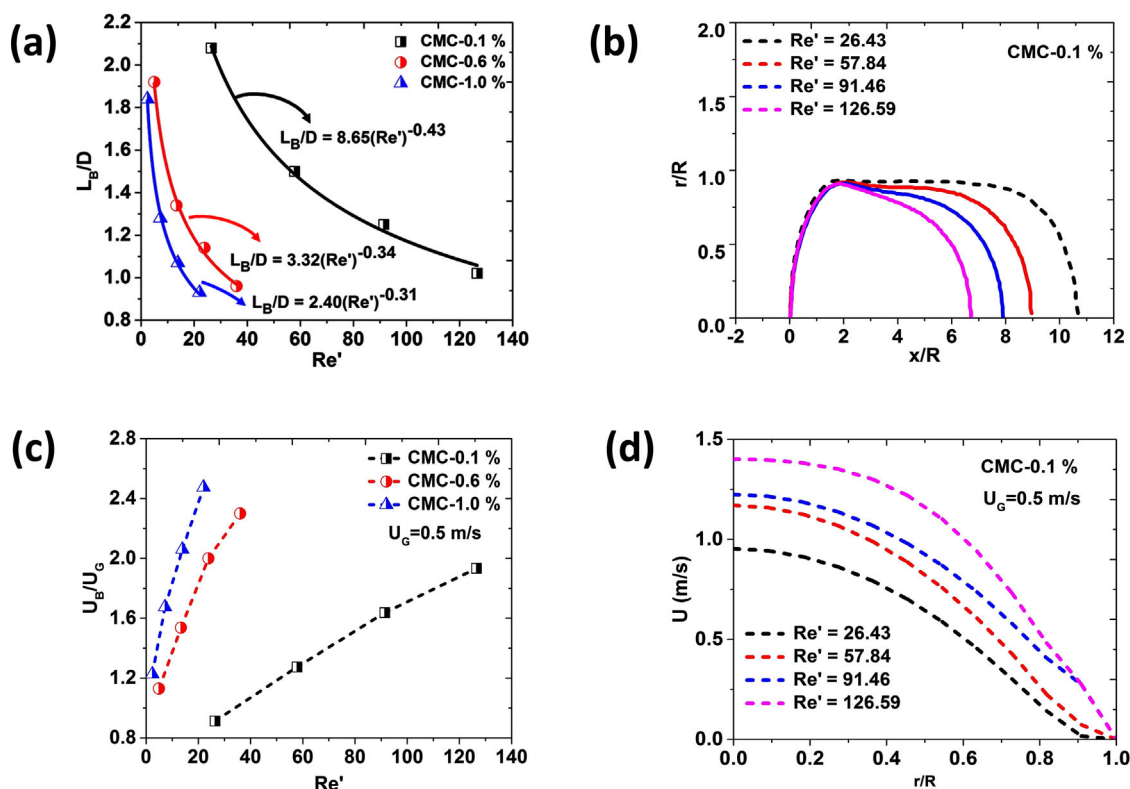
Figure 7. Effect of continuous phase velocity on: (a) non-dimensional bubble length, (b) Taylor bubble shape for CMC-0.1 %, (c) bubble velocity, and (d) velocity profiles inside Taylor bubble at U_G=0.5 m/s for CMC-0.1 %.

is closely associated with velocity field around the bubble, as shown in Figure 4. With increasing the CMC concentration, the effective viscosity magnitude increases around the Taylor bubble significantly increases, as shown in Figure 5d.

Additionally, a scaling relation is derived to determine the non-dimensional bubble length as a function of modified capillary number[47] $(Ca' = (\eta_0 - \eta_\infty)\lambda^{n-1}U^nD^{(1-n)}/\sigma)$ for the range of CMC concentration from 0.01–1.0 % (i.e., $Ca' = 0.037 - 0.602$) in Figure 6, where gas and liquid inlet velocities are kept constant at 0.5 m/s. The proposed scaling law relation $L_B/D = 1.23(Ca')^{-0.057}$ for different CMC solutions shows a maximum deviation of 1.2 %, and is in line with other non-Newtonian studies,[30,40] but with a different pre-factor and exponent.

Effect of Liquid Phase Velocity

In this section, the effect of liquid phase velocity of three different CMC concentration solutions on bubble length, velocity, shape, and velocity field inside the Taylor bubble are systematically studied. It can be observed from Figure 7a, that bubble length decreases with increasing liquid phase inlet velocity due to increase in inertial force on gas phase. Consequently, scaling relations are proposed for non-dimensional bubble length as a function of modified Reynolds number $(Re' = \rho U_L D/\eta_{eff})$, and are mentioned in Figure 7a. It can also be realized that the exponent and pre-factor of the proposed power-law relation change systematically with varying CMC concentration. It is worth mentioning that the proposed relations predict with a high degree of confidence, when the gas phase inlet velocity is kept constant at 0.5 m/s, as the Re' is calculated based on the liquid phase properties. At lower liquid velocity, a considerable change in the bubble length is observed for three different CMC liquids. The effect of

continuous inlet velocity on bubble shape is also analyzed for CMC-0.1 %. From Figure 7b, it can be seen that bubble nose shape significantly changes with increasing liquid phase inlet velocity. Consequently, Taylor bubble velocity increases due to significant change in bubble shape and film thickness (Figure 7c). Velocity inside the Taylor bubble also increases with enhanced continuous phase inlet velocity, as depicted in Figure 7d. This phenomenon is also attributed to the consequence of Taylor bubble shape and film thickness variation. For CMC-0.1 %, at lower liquid phase velocity, an elongated bubble and lower velocity field are observed inside the Taylor bubble.

At a fixed gas inlet velocity, the radius of bubble nose curvature becomes smaller, and the rear cap turns flatter with increasing liquid inlet velocity, as shown in Figure 8. It can also be noticed
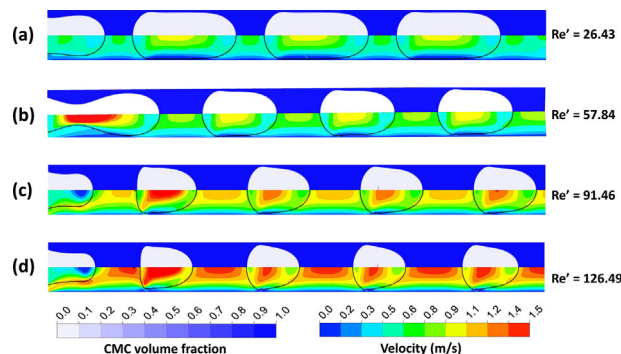

Figure 8. Effect of liquid flow rate on velocity distribution (upper halves are volume fraction and lower halves are velocity field) in CMC-0.1 % for fixed U_G = 0.5 m/s and at Re' = (a) 26.43, (b) 57.84, (c) 91.46, and (d) 126.49.
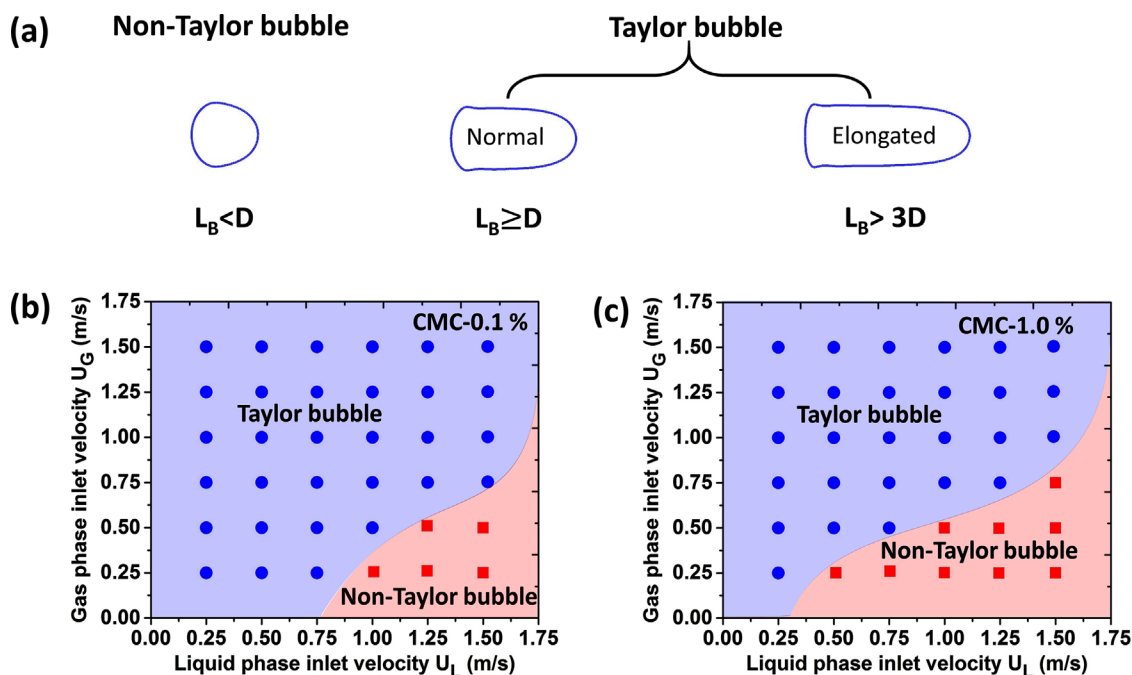
Figure 9. (a) Different shapes of Taylor bubbles, and flow regime map for (b) CMC-0.1 %, and (c) CMC-1.0 %.

from Figure 8 that velocity magnitude in the slug region, and in the middle of a bubble increases systematically with increasing liquid phase inlet velocity.

Flow Regimes Maps

In two-phase flow systems, knowledge of flow patterns is essential for understanding the behaviour of gas-liquid flows at a given operating condition. It can be recognized from the literature that reported flow regime maps in two-phase flows are typically valid for only Newtonian systems. Therefore, it is necessary to develop flow regime maps for gas-non-Newtonian liquid systems. Here, flow regimes are broadly categorized based on the bubble length into two main types such as, non-Taylor bubble and Taylor bubble. When Taylor bubble length is lower than the capillary diameter ($L_B < D$) is denoted as non-Taylor bubble and Taylor bubble length is higher than capillary diameter is denoted as Taylor bubble ($L_B > D$), as illustrated in Figure 9a. Flow regime maps for two different CMC solutions (CMC-0.1 and CMC-1.0 %) under various gas and liquid velocities are portrayed in Figure 9b and c, where the inlet velocities of the dispersed and continuous phases are used as the ordinate and abscissa, respectively. Figure 9b

shows that for lower CMC concentration (CMC-0.1 %), Taylor bubble regime occupies a larger area in the flow regime map and non-Taylor bubbles are mostly observed at higher liquid and lower gas-inlet velocities. However, with increasing concentration (CMC-0.1 %) the appearance of non-Taylor bubbles can be observed even at lower liquid inlet velocities, as shown in Figure 9c. In all cases, elongated Taylor bubbles are determined at higher gas inlet velocity, which is also labelled as Taylor bubble regime in this study (Figure 9a). It can be noted from Figure 9c, that with increasing CMC concentration, non-Taylor bubble regime expands as compared to a lower concentration of CMC solution (Figure 9b).

Effect of Surface Tension

Taylor bubble length and its formation strongly depend on the surface tension and viscous forces. In the open literature, several researchers have reported the effect of surface tension for gas-liquid system using sodium dodecyl sulphate (SDS) surfactant. To understand the role of surface tension in non-Newtonian system, we systematically investigate the effect of surface tension for shear thinning liquids by altering it from 0.072–0.042 N/m. Generally,
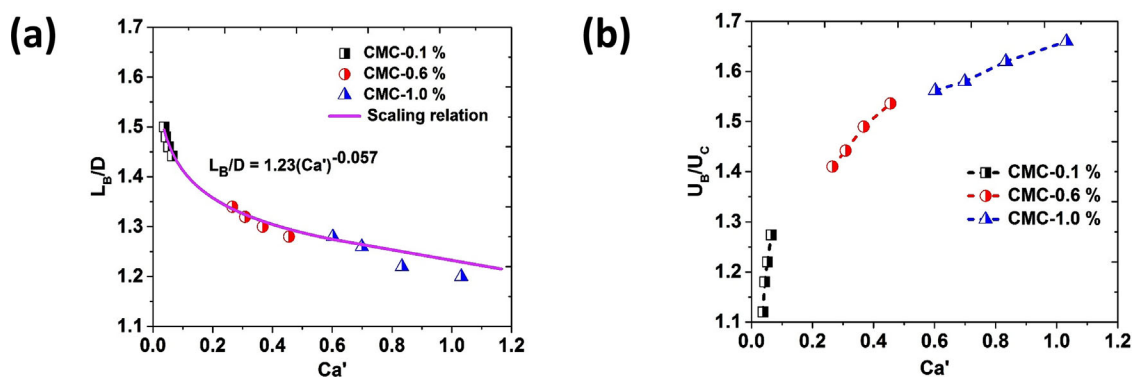

Figure 10. Effect of surface tension on: (a) non-dimensional bubble length, and (b) bubble velocity at U_L = 0.5 m/s, and U_G = 0.5 m/s.

at lower surface tension, weak interfacial forces will act on both phases. The non-dimensional bubble length (L_B/D) in all CMC solutions are plotted as a function of modified capillary number (Ca') in Figure 10a, which shows that with decreasing surface tension (i.e., increasing Ca'), bubble length decreases in all CMC solutions. This can be ascribed to the fact that at lower surface tension (higher Ca'), the growth of gas phase in the microchannel is hindered by higher shear force, which in turn results in smaller bubble length. It is worth noting that the scaling law proposed in Figure 6 corroborates predicted values here satisfactorily with a maximum deviation of 1.2 % in the range of $Ca' = 0.037 - 0.602$ for which it was developed. Interestingly, it also agrees well with a maximum deviation of 6.8 %, when it is extended for higher $Ca' = 1.03$. In line with the discussion in the previous section, bubble velocity, as depicted in Figure 10b, is found to increase in all CMC solutions due to the increase in liquid film thickness and alteration in bubble shape.

CONCLUSIONS

We have demonstrated characteristics of Taylor bubble flow in co-flow microchannels by considering carboxymethyl cellulose (CMC) as a liquid phase. A CFD model based on the VOF method is developed that helps in understanding the behaviour of Taylor bubble flow in Carreau-Yasuda shear thinning liquids. Systematic investigations are carried out to understand the effect CMC concentration, liquid phase inlet velocity, and surface tension on Taylor bubble length, velocity, shape, liquid film thickness, and velocity fields inside Taylor bubble, as well as in liquid slug. On increasing the CMC concentration and liquid phase inlet velocity, Taylor bubble length was found to decrease due to an increase in effective viscosity and inertial force, respectively. However, Taylor bubble velocity, liquid film thickness, and formation frequency increase with increasing CMC concentration and liquid phase inlet velocity. In this study, liquid film thickness is precisely captured for all the cases to understand its effect on the bubble characteristics. Influence of CMC concentration and liquid phase inlet on velocity distribution inside the Taylor bubble and liquid slug are also presented. Three different types of bubble shapes are identified, and the flow regime maps for Carreau-Yasuda liquids are developed for the first time, based on gas-liquid inlet velocities. On decreasing surface tension, the Taylor bubble length was observed to decrease but the velocity increased. To determine the bubble length, scaling laws are developed based on the modified capillary number, and Reynolds number that take into consideration of rheological properties, and flow rate, respectively. These findings are expected to serve as a basis for further experimental/numerical investigations with non-Newtonian liquids that may contribute in the design of microfluidic devices.

ACKNOWLEDGEMENTS

NOMENCLATURE

Ca'	modified capillary number ($(\eta_0 - \eta_\infty)\lambda^{n-1}U^n D^{(1-n)}/\sigma$)
Re'	modified Reynolds number ($= \rho U_L D/\eta_{eff}$)
D	diameter of the channel (m)
U	velocity (m/s)
L	length (m)
$\hat{N}$	unit normal vector
P	pressure (Pa)
C	volume fraction

Greek Symbol

$\dot{\gamma}$	shear rate (1/s)
δ	liquid film thickness (m)
η	dynamic viscosity (Pa . s)
ρ	density (kg/m³)
σ	surface tension (N/m)
$\bar{\bar{\tau}}$	shear stress (Pa)

Subscripts

B	bubble
G	gas
L	liquid
eff	effective

REFERENCES

[1] M. T. Kreutzer, F. Kapteijn, J. A. Moulijn, J. J. Heiszwolf, *Chem. Eng. Sci.* **2005**, *60*, 5895.

[2] Y. Liu, X. Jiang, *Lab Chip* **2017**, *17*, 3960.

[3] M. T. Kreutzer, F. Kapteijn, J. A. Moulijn, C. R. Kleijn, J. J. Heiszwolf, *AIChE J.* **2005**, *51*, 2428.

[4] A. Günther, K. F. Jensen, *Lab Chip* **2006**, *6*, 1487.

[5] R. S. Abiev, I. Lavretsov, *Chem. Eng. Sci.* **2012**, *74*, 59.

[6] Z. Pan, X. Zhang, Y. Xie, W. Cai, *Chem. Eng. Technol.* **2014**, *37*, 495.

[7] S. Irandoust, S. Ertlé, B. Andersson, *Can. J. Chem. Eng.* **1992**, *70*, 115.

[8] A. Kawahara, P.-Y. Chung, M. Kawaji, *Int. J. Multiphas. Flow* **2002**, *28*, 1411.

[9] P.-Y. Chung, M. Kawaji, *Int. J. Multiphas. Flow* **2004**, *30*, 735.

[10] H. Liu, C. O. Vandu, R. Krishna, *Ind. Eng. Chem. Res.* **2005**, *44*, 4884.

[11] W. Salman, A. Gavriilidis, P. Angeli, *Chem. Eng. Sci.* **2006**, *61*, 6653.

[12] M. van Sint Annaland, W. Dijkhuizen, N. Deen, J. Kuipers, *AIChE J.* **2006**, *52*, 99.

[13] C. W. Hirt, B. D. Nichols, *J. Comput. Phys.* **1981**, *39*, 201.

[14] M. van Sint Annaland, N. Deen, J. Kuipers, *Chem. Eng. Sci.* **2005**, *60*, 2999.

[15] M. Sussman, P. Smereka, S. Osher, *J. Comput. Phys.* **1994**, *114*, 146.

[16] Y. Sun, C. Beckermann, *J. Comput. Phys.* **2007**, *220*, 626.

[17] X. Shan, H. Chen, *Phys. Rev. E* **1993**, *47*, 1815.

[18] S. Shu, N. Yang, *Ind. Eng. Chem. Res.* **2013**, *52*, 11391.

[19] Z. Yu, O. Hemminger, L.-S. Fan, *Chem. Eng. Sci.* **2007**, *62*, 7172.

[20] Y. Chen, R. Kulenovic, R. Mertz, *Int. J. Therm. Sci.* **2009**, *48*, 234.

[21] F. Bretherton, *J. Fluid Mech.* **1961**, *10*, 166.

[22] D. Goel, V. V. Buwa, *Ind. Eng. Chem. Res.* **2008**, *48*, 8109.

[23] R. Gupta, D. F. Fletcher, B. S. Haynes, *Chem. Eng. Sci.* **2009**, *64*, 2941.

[24] Z. Wang, *Chem. Eng. J.* **2015**, *263*, 346.

[25] J. Azaiez, *Can. J. Chem. Eng.* **2007**, *85*, 251.

[26] R. Govindarajan, K. C. Sahu, *Annu. Rev. Fluid Mech.* **2014**, *46*, 331.

[27] P. Nghe, E. Terriac, M. Schneider, Z. Li, M. Cloitre, B. Abecassis, P. Tabeling, *Lab Chip* **2011**, *11*, 788.

[28] X. Frank, H. Z. Li, D. Funfschilling, F. Burdin, Y. Ma, *Can. J. Chem. Eng.* **2003**, *81*, 483.

[29] O. L. Hemminger, P. E. Boukany, S.-Q. Wang, L. Lee, *J. Non-Newton. Fluid* **2010**, *165*, 1613.

[30] T. Fu, Y. Ma, D. Funfschilling, H. Z. Li, *Chem. Eng. Process.* **2011**, *50*, 438.

[31] B. Chen, F. Guo, G. Li, P. Wang, *Chem. Eng. Technol.* **2013**, *36*, 2087.

[32] B. Laborie, F. Rouyer, D. E. Angelescu, E. Lorenceau, *Phys. Rev. Lett.* **2015**, *114*, 204501.

[33] S. Wang, J. Huang, K. He, J. Chen, *Int. J. Multiphas. Flow* **2011**, *37*, 1129.

[34] S. G. Sontti, A. Atta, *Ind. Eng. Chem. Res.* **2017**, *56*, 7401.

[35] S. G. Sontti, A. Atta, *Comput.-Aided Chem. En.* **2017**, *40*, 1201.

[36] M. Pathak, *J. Membrane Sci.* **2011**, *382*, 166.

[37] Z. Zhang, J. Xu, B. Hong, X. Chen, *Lab Chip* **2014**, *14*, 2576.

[38] Y. Ren, Z. Liu, H. C. Shum, *Lab Chip* **2015**, *15*, 121.

[39] Z. Lei, Y. Guo, C. Dai, L. Zi, B. Chen, *Catal. Today* **2016**, *276*, 150.

[40] S. G. Sontti, A. Atta, *Chem. Eng. J.* **2017**, *330*, 245.

[41] J. Brackbill, D. B. Kothe, C. Zemach, *J. Comput. Phys.* **1992**, *100*, 335.

[42] ANSYS Fluent, Release 17.0, Help system, Fluent Theory and User's Guide, ANSYS Inc., Canonsburg **2017**.

[43] P. J. Carreau, *Soc. Rheol.* **1972**, *16*, 99.

[44] R. Gupta, D. F. Fletcher, B. S. Haynes, *Chem. Eng. Sci.* **2010**, *65*, 2094.

[45] A. N. Asadolahi, R. Gupta, D. F. Fletcher, B. S. Haynes, *Chem. Eng. Sci.* **2011**, *66*, 5575.

[46] R. Sousa, M. Riethmuller, A. Pinto, J. Campos, *Chem. Eng. Sci.* **2005**, *60*, 1859.

[47] S. Shahsavari, G. H. McKinley, *Phys. Rev. E* **2015**, *92*, 063012.